

A combined study of thermohaline mixing and envelope overshooting with PARSEC: Calibration to NGC 6397 and M4

C. T. Nguyen^{1,2,*}, A. Bressan², A. J. Korn³, G. Cescutti¹, G. Costa⁴, F. Addari², L. Girardi⁵, X. Fu⁶,
Y. Chen⁷, and P. Marigo⁸

¹ INAF Osservatorio Astronomico di Trieste, Via Giambattista Tiepolo, 11, Trieste, Italy

² SISSA, Via Bonomea 265, I-34136 Trieste, Italy

³ Division of Astronomy and Space Physics, Department of Physics and Astronomy, Uppsala University, Box 516, SE-75120 Uppsala, Sweden

⁴ Univ Lyon, Univ Lyon1, ENS de Lyon, CNRS, Centre de Recherche Astrophysique de Lyon UMR5574, F-69230 Saint-Genis Laval, France

⁵ INAF Osservatorio Astronomico di Padova, Vicolo dell'Osservatorio n. 5, Padova, Italy

⁶ Purple Mountain Observatory, Chinese Academy of Sciences, Nanjing 210023, China

⁷ Anhui University, Hefei 230601, China

⁸ Dipartimento di Fisica e Astronomia, Università degli studi di Padova, Vicolo Osservatorio 3, Padova, Italy

Received 9 August 2024 / Accepted 3 March 2025

ABSTRACT

Thermohaline mixing is one of the main processes in low-mass red giant stars that affect the transport of chemicals and, thus, the surface abundances along the evolution. The interplay of thermohaline mixing with other processes, such as downward overshooting from the convective envelope, needs to be carefully investigated. This study aims to understand the combined effects of thermohaline mixing and envelope overshooting. After implementing the thermohaline mixing process in the PARSEC stellar evolutionary code, we computed tracks and isochrones (with the TRILEGAL code) and compared them with observational data. To constrain the efficiencies of both processes, we performed detailed modelling that is suitable for globular clusters NGC 6397 and M4. Our results indicate that an envelope overshooting efficiency parameter, $\Lambda_e = 0.6$, and a thermohaline efficiency parameter, $\alpha_{th} = 50$, are necessary to reproduce the red-giant-branch bump magnitudes and lithium abundances observed in these clusters. We find that both envelope overshooting and thermohaline mixing have a significant impact on the variation in ${}^7\text{Li}$ abundances. Additionally, we also explore the effects of adopting solar-scaled or α -enhanced mixtures on our models. The ${}^{12}\text{C}$ and the ${}^{12}\text{C}/{}^{13}\text{C}$ ratio are also effective indicators with which to probe extra mixing in red-giant-branch stars. However, their usefulness is currently limited by the lack of precise and accurate C-isotopes abundances.

Key words. stars: abundances – stars: evolution – stars: low-mass – stars: pre-main sequence

1. Introduction

Globular clusters (GCs) are well known to be formidable laboratories for studying the properties of stars in our Galaxy. These systems are populated by long-lived low-mass stars and their chemical composition varies from a very low metallicity to an almost solar one. They thus provide extremely useful information about the formation and evolution of the chemical elements of their birth clouds (Beers & Christlieb 2005; Frebel & Norris 2015). Furthermore, they are so populous that even the fastest stellar evolutionary phases can be seen and studied. They are thus an ideal test case with which to probe different physical processes that happen inside stars. One such process, the understanding of which is of paramount importance for building realistic stellar models, is internal mixing.

Due to the penetration of the convective envelope into the inner layers, during the first-ascent red-giant branch (RGB) mixing occurs between these two regions and leads to changes in surface abundance. This process is the so-called first dredge-up (1DU). In classical models, after the 1DU is completed, the surface abundances remain constant until the end of the RGB phase

(see Smith & Tout 1992; Charbonnel et al. 1998). However, measurements of the surface abundances of RGB stars show a different, more nuanced picture. For instance, Gratton et al. (2000) showed the variation of the many elements in field stars with $-2 < [\text{Fe}/\text{H}] < -1$, while Aguilera-Gómez et al. (2022) showed the trend of lithium abundances in five globular clusters. A striking example is the case of NGC 6397, where lithium abundances have been shown to have a significant drop after the RGB bump (Lind et al. 2009), along with carbon abundance (Briley et al. 1990). All measurements agree that extra mixing after the 1DU is required.

The process of thermohaline mixing has been studied in great detail by many authors. It was first introduced into stellar astrophysics by Ulrich (1972) and Kippenhahn et al. (1980). Later, Eggleton et al. (2006) investigated the instability regions inside low-mass stars and found a mean molecular weight inversion that explains the natural occurrence of thermohaline mixing by the reaction ${}^3\text{He}({}^3\text{He}, 2p){}^4\text{He}$ above the H-burning shell. Charbonnel & Zahn (2007a) established the importance of thermohaline mixing by showing the significant change in surface abundances of red giant stars after the bump. Since then, many investigations on the mixing scheme have been published.

* Corresponding author; chi.nguyen@inaf.it

For instance, Stancliffe et al. (2009) explored the effect of thermohaline mixing in carbon-normal and carbon-rich metal-poor giant stars (see also Stancliffe 2009; Placco et al. 2014); and Henkel et al. (2017, 2018) studied the modifications to the standard thermohaline mixing model. Other processes can affect the efficiency of thermohaline mixing; for example, rotation (Lagarde et al. 2011; Maeder et al. 2013) or magnetic field inhibit mixing in Ap stars (Charbonnel & Zahn 2007b).

Here, we want to investigate the interplay between convective envelope overshooting and the efficiency of thermohaline mixing, and how they impact the evolution of stars. For this purpose, we first implemented thermohaline mixing in the PARSEC stellar evolutionary code (Nguyen et al. 2022)¹ and calculated many low-mass models (in the mass range $0.64 \leq M/M_{\odot} \leq 0.94$) with four initial metallicities, $Z = 0.0001, 0.0002, 0.001, 0.002$ (in mass fraction), with variations in envelope overshooting and thermohaline mixing efficiencies, for which we adopted solar-scaled and $[\alpha/\text{Fe}] = 0.4$ -enhanced mixtures. We computed all models from the beginning of the pre-main-sequence (PMS) to the end of the RGB phase. The evolution of several chemical isotopes was followed during the entire evolution of the stars. The conversion from stellar evolutionary tracks to isochrones was done by using the TRILEGAL code (Girardi et al. 2005; Marigo et al. 2017)², which we modified to account for the additional isotopes ${}^7\text{Li}$ and ${}^{13}\text{C}$, to investigate the effect of thermohaline mixing.

The paper is organised into five sections. Section 2 shows the theoretical model of thermohaline mixing as a diffusive process and how we include it in our code, together with the input physics used in this work. The impact of thermohaline mixing on the evolution of the stellar model is presented here. We also discuss the role of the chemical compositions that are used in computing the models in this section. Then, Sect. 3 presents the calibration of the thermohaline efficiency parameter in which the variation in the predicted surface lithium abundance is directly compared to the observed data, and the calibration of envelope overshooting efficiency was based on the relative luminosity distance between the Li-peak and the onset of thermohaline mixing. Section 4 shows an independent calibration for the envelope overshooting efficiency parameter on the GC M4 based on the seismic data of RGB stars. Finally, we summarise and conclude this paper in Sect. 5.

2. PARSEC models with thermohaline mixing

2.1. Thermohaline mixing: Formalism

Thermohaline mixing sets in when an inversion of molecular weight (μ) arises in the interior of a star. The nuclear reaction of two ${}^3\text{He}$ to create one ${}^4\text{He}$ and two protons, ${}^3\text{He}({}^3\text{He}, 2p){}^4\text{He}$, below the convective envelope is the main mechanism that causes the instability regions of thermohaline mixing. However, in this study, we suggest that the inversion of the μ profile might also be caused by atomic ionisation throughout the star. This can be understood by the temperature distribution within a star. Namely, towards inner layers, the star has higher temperatures, which directly affect the ionisation degree of the chemical isotopes, which in turn directly affects the variation in molecular weight.

The physical process responsible for thermohaline mixing is double-diffusive instability, which was verified by

Charbonnel & Zahn (2007a). Instead, using a 3D hydrodynamics simulation, Eggleton et al. (2006) claimed that Rayleigh-Taylor instability is responsible. In either case, the instability happens in a stratified medium that satisfies the Ledoux criterion for convective stability, namely

$$\nabla_{\text{ad}} - \nabla + \left(\frac{\phi}{\delta}\right)\nabla_{\mu} > 0, \quad (1)$$

where the inversion in mean molecular weight, that is, $\nabla_{\mu} < 0$, must also occur. In the formula above, $\nabla_{\mu} = d \ln \mu / d \ln P$ is the molecular weight gradient, $\nabla = \partial \ln T / \partial \ln P$ is the temperature gradient, $\phi = (\partial \ln \rho / \partial \ln \mu)_{P,T}$ and $\delta = -(\partial \ln \rho / \partial \ln T)_{P,\mu}$ are the thermo-dynamical derivatives, and $\nabla_{\text{ad}} = P\delta/T\rho c_P$ is the adiabatic temperature gradient.

The mixing produced by thermohaline instability in radiative regions is described by the diffusion coefficient (see Cantiello & Langer 2010)

$$D_{\text{th}} = \frac{3}{2}\alpha_{\text{th}}K\frac{-\phi\nabla_{\mu}}{\nabla_{\text{ad}} - \nabla}, \quad \nabla_{\mu} < 0, \quad (2)$$

where $K = 4acT^3/3(c_P\kappa\rho^2)$ is the thermal diffusivity, in which a is the radiation density constant, c is the speed of light, c_P is the heat capacity at constant pressure, κ is the Rosseland mean opacity, and (ρ, T) are the stellar density and temperature; the dimensionless parameter α_{th} is a free parameter that controls the efficiency of thermohaline mixing. Therefore, the calibration of α_{th} is needed and it will be discussed in detail in Sect. 3. By comparing Eq. (2) with similar ones found in the literature, we obtain the relation

$$\alpha_{\text{th}} = \frac{2}{3}C_t = \frac{16}{9}(\pi^2\alpha^2), \quad (3)$$

where C_t and α are the thermohaline efficiency parameters used in Charbonnel & Zahn (2007a) and Ulrich (1972), respectively.

2.2. PARSEC models

We implemented the thermohaline mixing process in the latest version of PARSEC, V2.0 (Costa et al. 2019a,b; Nguyen et al. 2022; Costa et al. 2025). For the sake of brevity, we remind reader that the standard PARSEC V1.2S code is thoroughly described in Bressan et al. (2012), Chen et al. (2014), and Fu et al. (2018). In PARSEC V2.0, the nuclear reaction network includes the p-p chains, the CNO tri-cycle, the Ne-Na and Mg-Al chains, ${}^{12}\text{C}$, ${}^{16}\text{O}$, and ${}^{20}\text{Ne}$ burning reactions, and the α -capture reactions up to ${}^{56}\text{Ni}$, for a total of 72 different reactions that trace 32 isotopes: ${}^1\text{H}$, D , ${}^3\text{He}$, ${}^4\text{He}$, ${}^7\text{Li}$, ${}^7\text{Be}$, ${}^{12}\text{C}$, ${}^{13}\text{C}$, ${}^{14}\text{N}$, ${}^{15}\text{N}$, ${}^{16}\text{O}$, ${}^{17}\text{O}$, ${}^{18}\text{O}$, ${}^{19}\text{F}$, ${}^{20}\text{Ne}$, ${}^{21}\text{Ne}$, ${}^{22}\text{Ne}$, ${}^{23}\text{Ne}$, ${}^{23}\text{Na}$, ${}^{24}\text{Mg}$, ${}^{25}\text{Mg}$, ${}^{26}\text{Mg}$, ${}^{26}\text{Al}$, ${}^{27}\text{Al}$, ${}^{28}\text{Si}$, ${}^{32}\text{S}$, ${}^{36}\text{Ar}$, ${}^{40}\text{Ca}$, ${}^{44}\text{Ti}$, ${}^{48}\text{Cr}$, ${}^{52}\text{Fe}$, ${}^{56}\text{Ni}$, and ${}^{60}\text{Zn}$ (see Fu et al. 2018; Costa et al. 2021).

The major upgrade in PARSEC V2.0 is the inclusion of rotational effects with angular momentum transport and chemical mixing. Both processes are treated with purely diffusive schemes. The nuclear reactions and chemical variation equations are solved by the implicit method. The abundance variation includes nuclear reactions, turbulent motions, rotational mixing, and molecular diffusion (Costa et al. 2019b). The extra mixing produced by thermohaline is included in the code by adding the corresponding thermohaline mixing diffusion coefficient (Eq. (2)) to the turbulent one, which is included in the equation of chemical turbulent transport.

PARSEC accounts for mixing by convective overshooting beyond the Schwarzschild border, both in the core convective

¹ <http://stev.oapd.inaf.it/PARSEC/>

² <http://stev.oapd.inaf.it/cgi-bin/cmd>

region and at the bottom of the convective envelope. They are considered as radiative regions (for other approaches see Viallet et al. 2015 for reference). While the extension of the core overshooting region is determined by means of a ballistic approximation scheme (Bressan et al. 1981), the length of the overshooting region below the convective envelope region is parameterized as $L_{\text{EOV}} = \Lambda_e H_P$, with H_P being the pressure scale height and Λ_e the envelope overshooting parameter (see Alongi et al. 1991). Usually, the value adopted for Λ_e depends on the initial mass, which is $\Lambda_e = 0.5$ in low-mass stars ($M \leq 0.96 M_\odot$) and $\Lambda_e = 0.7$ in intermediate-mass stars ($M \geq 1.3 M_\odot$), with a linear transition between these two limits (Bressan et al. 2012; Nguyen et al. 2022). However, in this work, we let Λ_e as a free parameter that will be calibrated by comparing the models with observations (Sect. 4). In the PARSEC standard model, Λ_e , once it is indicated, is uniformly applied throughout the entire evolution of the stars. However, in Sect. 3.2, an attempt to use this parameter differently between the early- and post-MS phases is discussed in detail.

In the following sections, we compute a series of preliminary models of a typical low metallicity, $Z = 0.0002$, low-mass star, $M = 0.78 M_\odot$, with different adopting values of $\alpha_{\text{th}} = 50, 100, 150$ to analyse the efficiency of thermohaline mixing, and its impact on the stellar evolution. We will also adopt two different values of $\Lambda_e = 0.5$ and $\Lambda_e = 0.6$ to study the combined effects of envelope overshooting and thermohaline mixing.

2.3. Thermohaline instability region

Figure 1 depicts the run of the internal main quantities related to the thermohaline instability region at two evolutionary points along the RGB phase, that is, at a luminosity 0.5 dex dimmer and brighter than that of the RGB bump, respectively. In the stellar model located below the RGB bump (top-left panel), the mean molecular weight gradient, plotted in the top-left panel as $-\nabla_\mu$ with a dashed red line, is negative from the outer atmosphere layers until deep inside the star, at $M_r/M_{\text{tot}} \sim 0.47$, where the discontinuity in chemical distribution is located. We note that the chemical discontinuity, marked by the ${}^3\text{He}$ profile, is located below the Schwarzschild border indicated by the run of the radiative and adiabatic gradients because of envelope overshooting, which is illustrated by the grey-hatched area. In these chemically homogeneous layers, ∇_μ is negative because of the increasing ionisation degree. Below the chemical discontinuity, at about $M_r/M_{\text{tot}} \sim 0.47$ (see top-right panel), μ jumps to higher values, and ∇_μ becomes positive. In this model, the layers where the thermohaline diffusion coefficient, plotted by the solid yellow line, is larger than 0 are located between the chemical discontinuity and the Schwarzschild border, above which the region is convectively unstable. The borders of the thermohaline region are indicated by the cyan-shaded area in Fig. 1. However, it is important to note that if this region corresponds to the overshooting one, thermohaline mixing therefore has no effects. As can be seen, in this case, the two regions are superimposed.

In the model after the RGB bump (bottom-left panel), the H-burning shell has already erased the chemical discontinuity left by the first dredge-up. The region of efficient nuclear shell burning (grey-dotted area), marked by the steep decrease of the ${}^3\text{He}$ abundance, is much below the bottom envelope Schwarzschild border and cannot be reached even with overshooting mixing. However, in this region, the molecular weight is also sensitive to ${}^3\text{He}$ destruction by ${}^3\text{He}({}^3\text{He}, 2p){}^4\text{He}$ and ${}^3\text{He}({}^4\text{He}, \gamma){}^7\text{Be}$ reactions. Since, as shown in the figure, the ${}^3\text{He}({}^3\text{He}, 2p){}^4\text{He}$ reaction (solid green line) is faster than the ${}^3\text{He}({}^4\text{He}, \gamma){}^7\text{Be}$ one, an

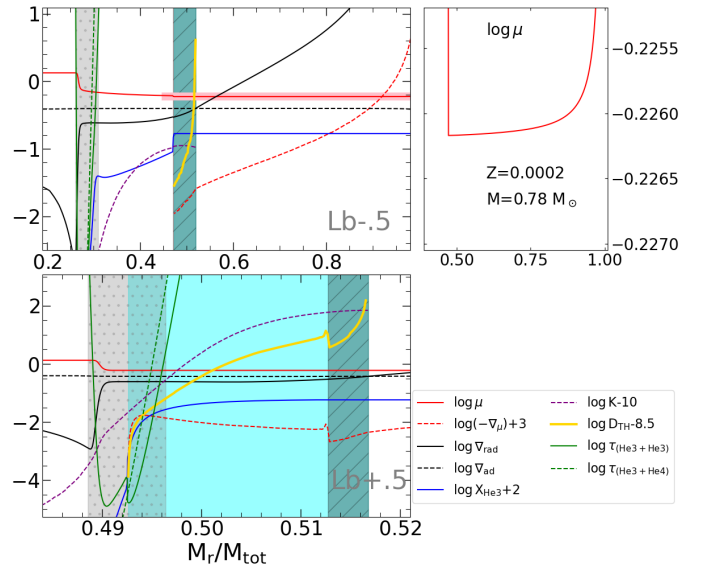


Fig. 1. Internal structure of the model with $Z = 0.0002$, $M = 0.78 M_\odot$, $\Lambda_e = 0.6$, and $\alpha_{\text{th}} = 50$. Top-left and bottom-left panels are the illustrations at the ± 0.5 dex point above and below the RGB-bump luminosity (Lb). The top-right panel is the zoom-in on the structure of $\log \mu$ at the outer layers, which is marked by the pink band on the top-left panel. The cyan-shaded area indicates the thermohaline instability. The grey-hatched area indicates the envelope overshooting region. The grey-dotted area indicates the H-burning shell. The green lines are the decay timescale of different reactions (in 10^8 yrs).

extended stratification with negative ∇_μ is produced between the ${}^3\text{He}$ -burning shell and the bottom of the envelope convective region. Thus, because of the thermohaline instability and envelope convection, ashes from the H-shell nuclear reactions can reach the stellar photosphere.

2.4. Effect of different efficiency values of α_{th}

We recall that in the current investigation, we have only investigated the effects of the thermohaline mixing process in the H-rich envelopes of RGB models. To see how the efficiency of the thermohaline mixing process varies along the RGB, in Fig. 2 we compare the internal variation of D_{th} at six typical stages along the evolution of the calculated models. The x-axis represents the mass fraction above the H-exhausted core relative to the mass of the inter-shell between the core and the convective envelope,

$$\delta M = \frac{M_r - M_c}{M_{\text{env}} - M_c}, \quad (4)$$

where M_r is the mass coordinate and M_{env} , M_c are the values at the base of the convective envelope, and where the hydrogen core mass fraction is $X_c < 10^{-7}$, respectively. Namely, $\delta M = 0$ marks the border of the inner core while $\delta M = 1$ marks the base of the envelope.

One can see that, as the star ascends the RGB, the thermohaline mixing process becomes more efficient, with D_{th} increasing by order of magnitudes, with α_{th} modulating its efficiency. The growth of D_{th} is due to the rapid increase of thermal diffusivity, K , due to the decrease in mass density during the evolution of red giant stars. For example, in models with the same $\alpha_{\text{th}} = 50$ (see Fig. 1), $\log D_{\text{th}}$ changes from 0.66 dex (Lb-0.5 model) to 2.22 dex (Lb+0.5 model) at the Schwarzschild border, while the thermal diffusion coefficient changes from 9.034

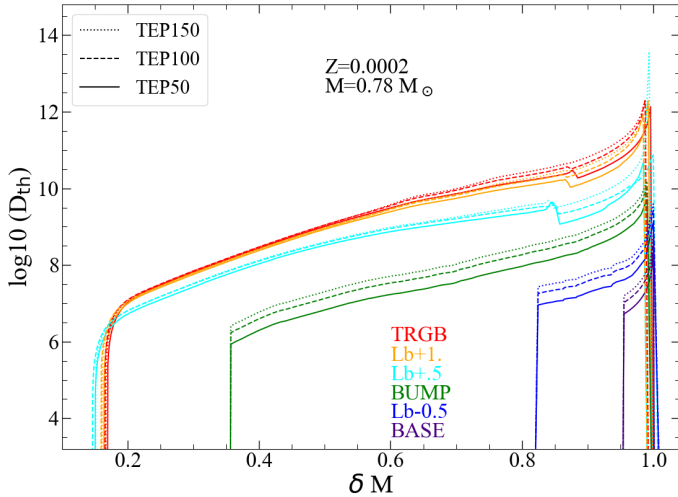


Fig. 2. Variation of thermohaline diffusion coefficient within the radiative region, at five typical stages along the evolution of a selected star, $0.78 M_{\odot}$. The x-axis is the relative mass in Eq. (4). Models with different thermohaline efficiency parameters, $\alpha_{\text{th}} = 50, 100, 150$, (referred to as ‘TEP’) are displayed with different line styles, while colours indicate the five stages: at the base of the RGB (BASE), 0.5 dex below the bump’s luminosity (Lb-0.5), at the bump’s luminosity (BUMP), 0.5 dex above the bump (Lb+0.5), 1 dex above the bump (Lb+1), and at the tip of the RGB (TRGB).

Table 1. Location and size of the RGB bump, together with the luminosity and age at the tip of the RGB of a given model with $0.78 M_{\odot}$, $Z = 0.0002$ and for four values of $\alpha_{\text{th}} = 0-150$, and two sets of models with $\Lambda_e = 0.5$ and 0.6 .

	$\log L_{\text{avg}}$	$\Delta \log L_{\text{bump}}$	$\log L_{\text{tip}}$	t_{tip} (Gyr)
$\Lambda_e = 0.5$				
$\alpha_{\text{th}} = 0$	2.04906	0.00622	3.34714	13.43002
$\alpha_{\text{th}} = 50$	2.05257	0.00776	3.33226	13.42805
$\alpha_{\text{th}} = 100$	2.05470	0.00948	3.33211	13.42798
$\alpha_{\text{th}} = 150$	2.05591	0.01072	3.33128	13.42792
$\Lambda_e = 0.6$				
$\alpha_{\text{th}} = 0$	2.02502	0.00673	3.34710	13.43035
$\alpha_{\text{th}} = 50$	2.02877	0.00796	3.33321	13.42829
$\alpha_{\text{th}} = 100$	2.03070	0.00937	3.33188	13.42818
$\alpha_{\text{th}} = 150$	2.03214	0.01114	3.33109	13.42811

dex to 11.86 dex correspondingly. This can be understood by the inverse relation of thermal diffusivity with density. In other words, the expansion during the giant phase leads to a significant decrease in the density and hence to a rise in thermal diffusivity, and so in D_{th} . Another interesting point is that the instability region grows in size (in terms of relative mass), from the base of the envelope to the H-burning shell region, along the evolution of the stars. Finally, the strength of thermohaline directly depends on its efficiency parameter, that is, the larger α_{th} , the higher D_{th} . As a consequence, the additional mixing directly changes the distribution of chemical elements and, eventually, the further evolution of the stars during the RGB.

Concerning the differences in the Hertzsprung–Russell diagram (HRD), in Table 1 we compare the average luminosity of the bump between the maximum and minimum values ($\log L_{\text{avg}}/L_{\odot}$), the size of the bump in terms of $\log L/L_{\odot}$ (meaning, the difference between the minimum and maximum lumi-

nosity of the bump), and the luminosity and age at the tip of the RGB phase. A larger value of α_{th} leads to a slightly more luminous RGB bump and to a slightly larger difference between the minimum and maximum luminosity of the bump, which, in turn, leads to a slightly lower RGB tip luminosity and a younger RGB tip age. However, it should be emphasised that the differences here are rather modest. As expected, changing Λ_e has a more significant impact, especially on the location of the bump. A typical value seen from our model’s prediction is about 0.024 dex difference between the $\Lambda_e = 0.5$ and 0.6 models. Meanwhile, estimation from observation establishes that a typical value of the magnitude dispersion of the RGB bump in the low metallicity domain is about 0.03 dex (see Nataf et al. 2013), which corresponds to ~ 0.012 dex dispersion in luminosity.

2.5. Chemical abundances

Since thermohaline mixing can convey elements from the inner H-shell to the base of the outer convective envelope, its largest effect is expected to appear in the abundance evolution of those elements, particularly at the stellar surface. In Fig. 3, we show the structure of ten chemical elements from ^1H to ^{18}O in the radiative zone between the central core and the envelope of a star $0.78 M_{\odot}$, $Z = 0.0002$, at the same five stages of Fig. 2.

At the base of the RGB phase, ^3He accumulates as a result of the pp-chain nuclear reaction from the main sequence and reaches its peak in the shells above the central core. It is brought up to the convective envelope at first and then transported down to the region of the H-burning shell due to the 1DU later on.

In the deeper layers, the variations in ^{12}C and ^{13}C result from the competition between $^{12}\text{C}(^1\text{H},\gamma)^{13}\text{N}(e^+ + \nu_e)^{13}\text{C}$ and $^{13}\text{C}(^1\text{H},\gamma)^{14}\text{N}(^1\text{H},\gamma)^{15}\text{O}(e^+ + \nu_e)^{15}\text{N}(^1\text{H},^4\text{He})^{12}\text{C}$ via the CNO-I cycle. In deeper layers, the depletion of ^{17}O and ^{18}O results from the ON cycle that enriches ^{16}O and creates its plateau. The variation of ^{14}N and ^{15}N is also a consequence of the competition between those nuclear processes.

Further towards the RGB bump, at which the penetration of the convective envelope has its maximum extension, ^3He is already engulfed down to the H-burning shell regions. Up to this point, the inner temperature is high enough to ignite the ^3He reactions and enlarge the region of thermohaline instability. During further evolution up to the tip of the RGB, the efficient thermohaline region increases in size, and mixes the inner layers above the H-burning shell with the external envelope. As a consequence, thermohaline mixing enriches the abundance of ^{14}N while ^{12}C and ^{13}C and ^{15}N are depleted. Overall, throughout the whole RGB phase, thermohaline mixing results in a depletion of the surface abundance of ^3He , ^7Li , ^{12}C , ^{13}C , ^{15}N , ^{18}O , ^{19}F , and ^{22}Ne , and an increase of ^{14}N , ^{17}O , and ^{23}Na , while the surface abundances of other heavier elements remain unaffected because they are not involved in nuclear reactions at this early stage of evolution.

Of particular interest is the surface abundance evolution of ^3He , ^7Li , ^{12}C , and ^{13}C during the RGB phase. The first element drives the thermohaline process, while the abundance of the other elements is commonly used to probe the internal mixing of low-mass giant stars by comparing their observed values.

Figure 4 shows the evolution of the surface abundances³ of ^3He , ^7Li , ^{12}C and C-isotopic ratio⁴, as a function of the stellar luminosity for a star with $M = 0.78 M_{\odot}$, $Z = 0.0002$, and different assumptions of the envelope overshooting and thermohaline

³ $A(X) = \log(n_X/n_H) + 12$.

⁴ $^{12}\text{C}/^{13}\text{C} = n_{^{12}\text{C}}/n_{^{13}\text{C}}$.

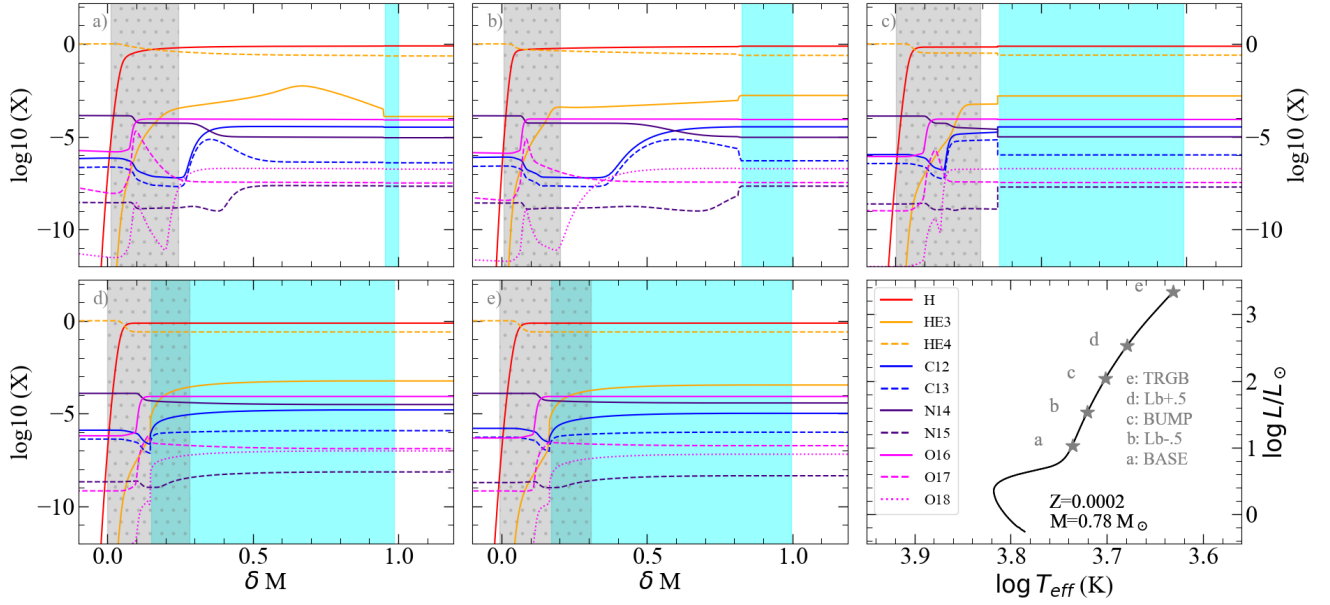


Fig. 3. Variation of chemical elements from ^1H to ^{18}O in five stages along the RGB phase of a selected star with initial mass $0.78 M_{\odot}$ and metallicity $Z = 0.0002$. The HRD of the corresponding star begins from the zero-age main sequence, with the five marked stages. Each element is indicated by the coloured lines. The cyan-shaded area displays the thermohaline instability region at each evolutionary stage (bottom-right panel), the grey-dotted area indicates the H-burning shell. All first five panels share the same scale on the x - and y -axis.

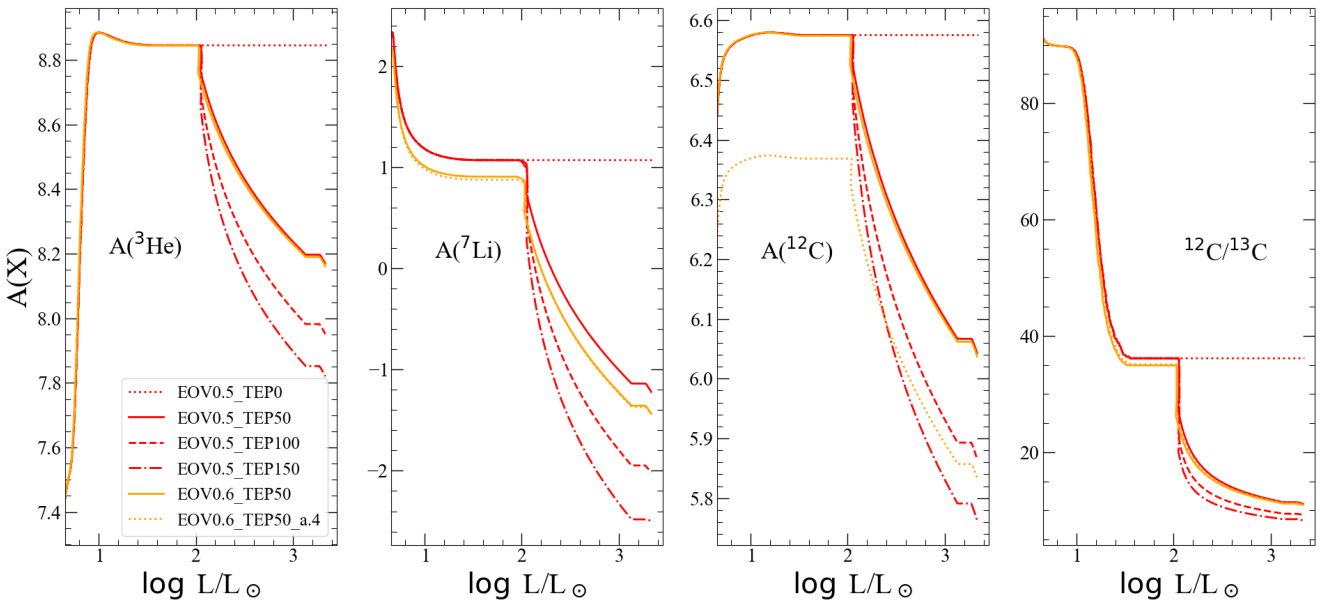


Fig. 4. Comparison between different models of the variation surface abundances of ^3He , ^7Li , ^{12}C , and C-isotopes ratio. The models with different values of $\Lambda_e = 0.5, 0.6$, and $\alpha_{\text{th}} = 0, 50, 100, 150$ by using solar-scaled and $[\alpha/\text{Fe}] = 0.4$ mixtures are shown according to the indicated labels. For simplicity, only the evolution during the red giant phase is shown here.

parameters, as indicated in the caption. The first hump of the ^3He abundance at $\log L \sim 1$ is the result of IDU. Corresponding with this hump, we note a strong decrease of ^7Li , an increase of ^{12}C , and a plateau in the $^{12}\text{C}/^{13}\text{C}$ abundance ratio. The following variation up to $\log L \sim 1.3$ is produced by the further penetration of envelope convection up to its maximum depth. After that, surface abundances remain unchanged while, in the meantime, the H-burning shell advances until it reaches the discontinuity left by the maximum penetration of envelope convection. This happens at the RGB bump at $\log L \sim 2$ for the adopted models. It is worth noting the barely visible variation in the RGB

bump luminosity and the more conspicuous effect on $A(^7\text{Li})$ and the $^{12}\text{C}/^{13}\text{C}$ ratio, which are produced by the different assumptions of envelope overshooting efficiency. These points will be discussed in more detail in Sect. 3.

As the H-shell moves forward to the discontinuity, which remains very near to the base of the convective envelope but without thermohaline circulation (model EOV0.5_TEP0, dotted red line), there will be no further mixing between these two regions. However, in the presence of thermohaline, the mixing continues with an efficiency that strongly depends on the thermohaline efficiency parameter (Charbonnel & Zahn 2007a;

Cantiello & Langer 2010). Finally, we can see how the variation in ^{12}C is due to mixing compared to its variation due to α -enhancement.

From the above discussion, we conclude that the envelope overshooting efficiency establishes the location of the H discontinuity in the interior structure, and thus the luminosity of the RGB bump. It also affects the surface abundance of Li at the RGB. On the other hand, the efficiency of thermohaline mixing drives the subsequent depression of $A(^7\text{Li})$, $A(^{12}\text{C})$, and of the $^{12}\text{C}/^{13}\text{C}$ ratio (see also Henkel et al. 2017; Aguilera-Gómez et al. 2023, and references therein). In the next sections, we use these two different effects to disentangle the two processes and to calibrate the thermohaline and envelope overshooting efficiency parameters.

3. Distance-independent calibration of α_{th} and Λ_e from Li-abundance in NGC 6397

In order to constrain the thermohaline efficiency parameter α_{th} in Eq. 2, we compare our model predictions with the ^7Li abundance of 349 stars of the metal-poor GC NGC 6397 from Lind et al. (2009), and the ^{12}C abundances from Briley et al. (1990). Furthermore, the relative distance between the Li-peak on the sub-giant and the location of the RGB bump implies a robust calibrator for envelope overshooting. These are discussed in detail below.

3.1. Li-abundances and thermohaline mixing

NGC 6397 is one of the most metal-poor GCs. Determination of its metallicity has been pursued in many works; for instance, Gratton et al. (2003) estimate the metallicity to be $[\text{Fe}/\text{H}] = -2.03 \pm 0.05$, Lind et al. (2009) determine $[\text{Fe}/\text{H}] = -2.10$, while Korn et al. (2007) find $[\text{Fe}/\text{H}] = -2.28 \pm 0.04$ for turn-off stars and $[\text{Fe}/\text{H}] = -2.12 \pm 0.03$ for RGB stars, the difference being attributed to atomic diffusion. The distance modulus of NGC 6397 has also been studied in many individual works, from the colour-magnitude diagram (CMD) fitting to kinematic simulations and parallax analysis. For instance, Reid & Gizis (1998), Gratton et al. (2003), Hansen et al. (2007), Valcin et al. (2020), and Gontcharov et al. (2023) report an estimated distance of about ~ 2.46 – 2.67 kpc by using CMD fitting. Also using the CMD fitting method, Correnti et al. (2018) derive a distance of 12.02 ± 0.03 mag (~ 2.53 kpc). The N-body model-fitting method performed in Baumgardt et al. (2019) for 154 Galactic GCs gives a distance of 2.45 ± 0.04 kpc for NGC 6397. A trigonometric parallax analysis of the cluster by Brown et al. (2018) gives a distance of 2.39 ± 0.17 kpc, taking into account contributions from both statistical and systematic errors, and Baumgardt & Vasiliev (2021) give a mean distance of 2.482 ± 0.019 kpc. We notice that differences in the adopted distance modulus can lead to a reasonably uncertainty of ~ 0.1 dex to the derived luminosity for NGC 6397. The age of this cluster is estimated to lie between 12.5–13.5 Gyr within the estimated uncertainties (see Gratton et al. 2003; Dotter et al. 2010; VandenBerg et al. 2013; Correnti et al. 2018; Tailo et al. 2020; Ahumada et al. 2021). The turn-off mass is about $0.78 M_{\odot}$ (see Korn et al. 2007).

We adopt the lithium abundance of a total of 349 stars spanning from the main-sequence (MS) turn-off point to the RGB from Lind et al. (2009) for the purpose of calibration. Recently, Wang et al. (2021) have provided a grid of synthetic spectra and abundance corrections taking into account the combined effect

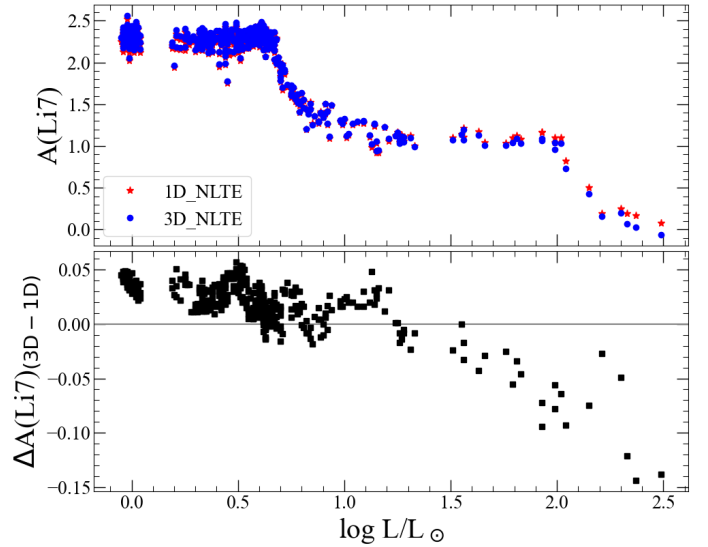


Fig. 5. Comparison of $A(^7\text{Li})$ in GC NGC 6397 using 3D and 1D NLTE corrections. Top-panel: Derived abundances of all stars in the Lind et al. sample. Bottom-panel: Difference in $A(^7\text{Li})$ between the two methods.

from 3D+NLTE, which is provided in the BREIDABLIK package⁵. Taking advantage of this more recent update, we re-derived the abundance of all stars in the Lind et al. sample from their reported equivalent widths and used them in this work. The comparison between data derived with 3D and 1D NLTE corrections is shown in Fig. 5 for all stars from the dwarf-MS to red giants. We find that for those stars below the RGB bump, there is an abundance shift of at most $\sim +0.05$ dex between the 3D and 1D NLTE corrections. For those stars located above the bump, the difference tends to increase up to a value of ~ -0.15 dex. Most importantly, the corrections in the two domains have different signs, which change the overall trend.

Among 90 RGB stars, there are seven stars located at the luminosity above the RGB bump, which requires an extra mixing to be reproduced (see Korn et al. 2007; Henkel et al. 2017). In Fig. 6, we compare the variation of $A(^7\text{Li})$ along the evolution of stellar models of $M = 0.78 M_{\odot}$ and $Z = 0.0002$ with the data, which is appropriate for the early post-MS evolution of NGC 6397. While it is well known that the 1DU event is responsible for the first falling branch in the low-luminosity domain around the RGB base in Fig. 6, in standard models (with no extra mixing and $\alpha_{\text{th}} = 0$, model EO0.5_TEP0) the abundance of ^7Li remains constant after the bump since there is no further mixing. However, in the presence of thermohaline mixing, ^7Li diffuses downward from the envelope, which leads to the second falling branch above the RGB bump. Here, we would like to stress that it is difficult to draw firm conclusions from the four most luminous stars in the Lind et al. (2009) sample because they only have upper limits on the ^7Li abundance. Therefore, we chose the three stars that are nearest to the bump as our best-fit constraint (circled in green). Indeed, the lithium abundance of these three stars is very well predicted by our model with $\alpha_{\text{th}} = 50$.

Besides that, in Fig. 6 we show the models that are calculated with an envelope overshooting efficiency parameter of $\Lambda_e = 0.5$, which is the value used in PARSEC v2.0 models, and a higher value of $\Lambda_e = 0.6$. As can be seen, $A(^7\text{Li})$ changes significantly when the efficiency of envelope overshooting is changed. In contrast, the variation in ^7Li abundance is very

⁵ <https://github.com/ellawang44/Breidablik>

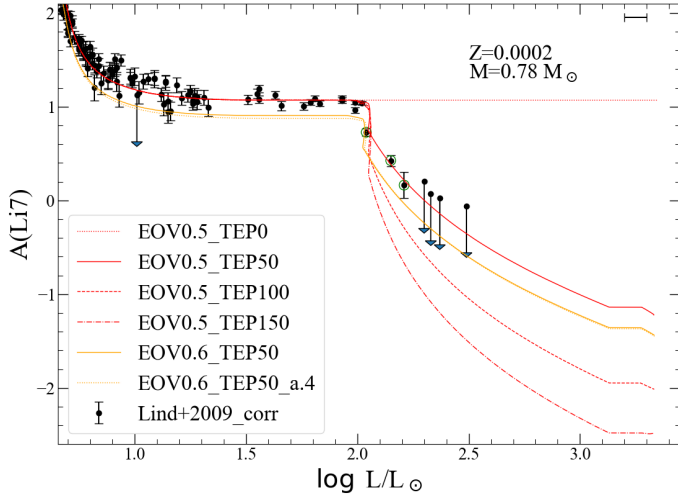


Fig. 6. Variation of ${}^7\text{Li}$ abundance versus luminosity of giant stars. The computed track with $\Lambda_e = 0.5$ and solar-scaled mixture is shown in red, with four values of $\alpha_{\text{th}} = 0, 50, 100, 150$ shown by different line styles. The yellow lines show tracks with $\Lambda_e = 0.6$, $\alpha_{\text{th}} = 50$ using solar-scaled mixture (solid) and $[\alpha/\text{Fe}] = 0.4$ mixtures (dotted). The error bar in the upper right indicates the typical 0.1 dex uncertainty in $\log L$.

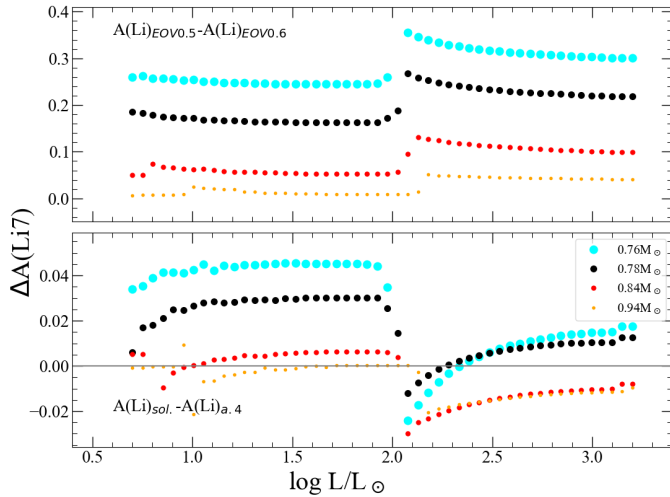


Fig. 7. Difference in $A({}^7\text{Li})$ between models in Fig. 6. Top-panel: Difference between track with $\Lambda_e = 0.5$ and $\Lambda_e = 0.6$, by using the solar-scaled mixtures. Bottom-panel: Difference between track using solar-scaled and α -enhanced mixtures, with the same value $\Lambda_e = 0.6$.

similar between models computed with solar-scaled and α -enhanced mixtures. To better understand this point, Fig. 7 shows the differences in $A({}^7\text{Li})$ between models with $\Lambda_e = 0.5$ and models with $\Lambda_e = 0.6$ (top panel), and between models with solar-scaled and α -enhanced mixtures (bottom panel) for a few models with a given initial mass. In the case of the $0.78 M_{\odot}$ model, a minimum of ~ 0.16 dex difference is found when varying Λ_e from 0.5 to 0.6 at the early phase below the bump. The discrepancy tends to be larger after the bump, with a maximum difference of about ~ 0.3 dex. The absolute value of the change also depends on the initial mass, as shown in the figure. Namely, the higher the mass, the smaller the difference. On the other hand, the maximum difference between the two models of using solar-scaled and $[\alpha/\text{Fe}] = 0.4$ -mixtures is ~ 0.04 dex, in all models, as can be seen in the bottom panel.

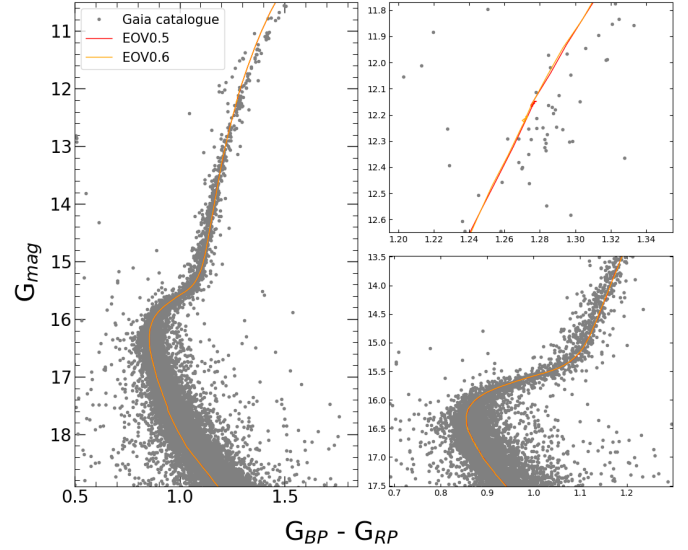


Fig. 8. Colour-magnitude diagram of GC NGC 6397 in Gaia DR3 pass-bands. The data is taken from the Gaia EDR3 catalogue (Vasiliev & Baumgardt 2021). The isochrones are shown with the adopted parameters $(m - M)_0 = 12.05$ mag, $[\text{Fe}/\text{H}] = -2.088$, $A_V = 0.58$ mag, and age $t = 12.8$ Gyr. The two panels on the right-hand side are zoomed-in on the bump and main-sequence areas.

For a more refined calibration, we computed several low-mass models, in the range of masses $M = 0.64\text{--}0.94 M_{\odot}$, for two initial metallicity sets, $Z = 0.0001, 0.0002$, with the $[\alpha/\text{Fe}] = 0.4$ mixture. For each metallicity set, we computed models with both values of $\Lambda_e = 0.5$ and 0.6 and a value of $\alpha_{\text{th}} = 50$. All models were set up with an initial lithium value of $A({}^7\text{Li}) = 2.72$. Additionally, we also computed a set with $\Lambda_e = 0.6$ and $\alpha_{\text{th}} = 100$, and a set with $\Lambda_e = 0.05$ and $\alpha_{\text{th}} = 50$ for the sake of comparison. Then, together with our newly computed models, we adopted the very-low-mass models⁶ ($M \leq 0.60 M_{\odot}$) from the PARSEC v1.2s dataset⁷ to produce the corresponding isochrones. The isochrones are produced by the recent version of the TRILEGAL code (more details of the interpolation scheme can be found in Girardi et al. 2005; Marigo et al. 2017; Bertelli et al. 1990, 2008) and converted into the photometric magnitudes by using the YBC table⁸ (Chen et al. 2019).

As the first step in the analysis, Fig. 8 shows the observed CMD of GC NGC 6397 in Gaia DR3 pass-bands, superimposed with our isochrones ($\alpha_{\text{th}} = 50$). We note that, for simplicity, the isochrones are limited up to the tip of the RGB phase. In Fig. 8, we adopt the distance modulus $(m - M)_0 = 12.05$ mag from Correnti et al. (2018), and initial the metallicity $Z = 0.0002$ ($Y = 0.249$, which corresponds to $[\text{Fe}/\text{H}] = -2.088$ with $[\alpha/\text{Fe}] = 0.4$). Our best-fit isochrones imply an extinction of $A_V = 0.58$ mag and an age of 12.8 Gyr, which are in good agreement with the literature (Correnti et al. 2018; Gontcharov et al. 2023, and others). Overall, our isochrones perform well, yielding a global fit from the low-MS part up to the lower red-giant branch of the cluster. Furthermore, the location of the bump

⁶ Very-low-mass stars undergo central hydrogen burning for timescales that exceed the age of the universe. Consequently, these stars do not experience thermohaline mixing, which allows us to use stellar evolutionary tracks that omit thermohaline mixing to construct our isochrones.

⁷ http://stev.oapd.inaf.it/PARSEC/tracks_v12s.html

⁸ <http://stev.oapd.inaf.it/YBC/>

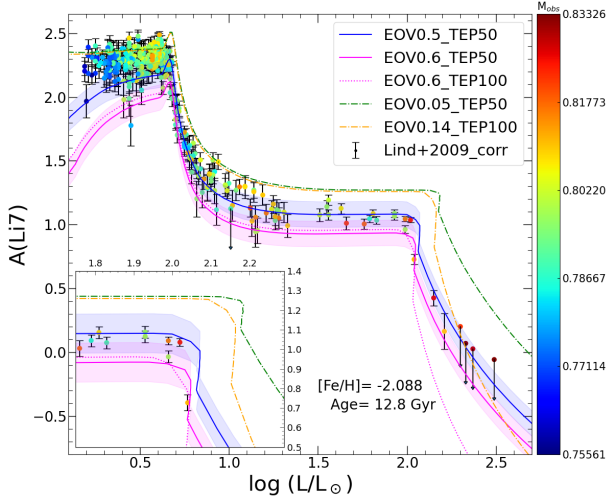


Fig. 9. Isochrone fitting of the observed ${}^7\text{Li}$ -abundance data. The model that gives the best CMD fit in Fig. 8 is compared to the 3D+NLTE-corrected data from Lind et al. (2009). Models with ($\Lambda_e = 0.6$, $\alpha_{\text{th}} = 100$), ($\Lambda_e = 0.14$, $\alpha_{\text{th}} = 100$), and one with ($\Lambda_e = 0.05$, $\alpha_{\text{th}} = 50$) are also plotted here for the sake of comparison. The insert panel zooms in on the onset of thermohaline mixing. The colour bar indicates the observed masses (Masses are derived from g , T_{eff} , and L values provided by Lind et al. 2009.).

selects the best-fitting model with $\Lambda_e = 0.6$ and $[\alpha/\text{Fe}] = 0.4$ -mixture. The upper branch of the RGB shows an offset from the observed data, which is a problem seen in many globular clusters (Cohen et al. 2015). The discrepancy could be due to many physical factors that are used in computing the stellar models, such the efficiency of convective energy transport (mixing-length parameter, density inversion, etc.), diffusion, mass loss, or systematic errors in the adopted bolometric corrections and metallicity (see Vandenberg et al. 2013; Correnti et al. 2018). On this note, we recall that PARSEC’s standard prescriptions for these physical processes are used in this work (see Sect. 2.2). A thorough analysis of this problem is beyond the scope of this work and will be addressed in a coming work.

After obtaining constraints on the photometric properties from the CMD fit, we proceed to the comparison with the observed ${}^7\text{Li}$ -abundance trend. Figure 9 shows the re-derived 3D+NLTE lithium abundances and the variation in $A({}^7\text{Li})$ from our models versus luminosity. It should be noted that the models shown in Fig. 9 are obtained from the best-fitting CMD above. We also include a model with $\alpha_{\text{th}} = 100$ in the plot for the sake of comparison. Investigating the comparison, one can see that the shape of lithium depletion after the RGB bump is the feature that verifies the constraint on the efficiency of thermohaline mixing. A reasonable uncertainty of ± 0.1 dex due to the absolute value of $A({}^7\text{Li})$ from the previous phases claims the best-fitted value is $\alpha_{\text{th}} = 50$. The model with $\alpha_{\text{th}} = 100$ enhances the efficiency of thermohaline mixing too much. It is also clear that high overshoot efficiencies engulf the surface lithium too much during the early MS; on the contrary, the observed data show a well-known Spite-plateau. This point will be further discussed in the next sub-section. Despite this, the location of thermohaline’s onset (in $\log L$) shows its best-fit to the model with $\Lambda_e = 0.6$.

Furthermore, we also include in Fig. 9 the model with $\Lambda_e = 0.05$. By changing the efficiency, Λ_e , the RGB bump’s location changes significantly; for example, an ~ 0.15 dex difference (in $\log L$) can be seen between the models with $\Lambda_e = 0.05$ and 0.6 . In the meantime, the location of the Li peak on the sub-giant

branch remains almost unchanged between models (≤ 0.005 dex difference). This result will be revisited in detail below.

Finally, for comparison, our best-fitting thermohaline efficiency parameter is lower than the result of Henkel et al. (2017) who get $C_t = 150$, while our results indicate $\alpha_{\text{th}} = 50$, which corresponds to $C_t = 75$. We also notice that their models use an envelope overshooting value of $0.14H_p$ while in this work we calibrate and use a higher value, either $\Lambda_e = 0.5$ or 0.6 . The orange line in Fig. 9 represents our model computed with their best-fit parameters ($\Lambda_e = 0.14$, $\alpha_{\text{th}} = 100$). However, we should emphasise that a comparison between stellar codes could be challenging due to differences in methodology and input physics; dedicated work on this matter is therefore beyond the scope of this paper and worth a separate study in the near future.

3.2. Spite plateau

The predicted amount of lithium formed in the early universe is up to three times larger than the observed abundance in halo field and globular-cluster stars (e.g. Charbonnel & Primas 2005; Bonifacio 2002; Korn et al. 2007). For instance, Spite & Spite (1982a,b) showed that old stars in a certain range of effective temperatures display a similar amount of lithium ($A(\text{Li}^7) \approx 2.2$), making up the so-called Spite plateau (see also, Spite & Spite 2010). Coc et al. (2012) used the measured number of baryons per photon from the Wilkinson Microwave Anisotropy Probe satellite (Komatsu et al. 2011) to constrain the primordial value $A(\text{Li}^7) \approx 2.72$ dex. Later on, Coc et al. (2014) updated their results by using the cosmological parameters determined by Planck (Planck Collaboration XVI 2014), which resulted in a slightly lower average value, $A(\text{Li}^7) \approx 2.69^{+0.04}_{-0.03}$ dex. The discrepancy between the measured $A(\text{Li}^7)$ and its prediction from Big Bang nucleosynthesis is known as the ‘cosmological lithium problem’.

As shown in the section above, applying a high-efficiency value of envelope overshooting during the early MS might lead to an over-depletion of lithium in the Spite-plateau area. Indeed, Christensen-Dalsgaard et al. (2011) investigated the convective envelope overshooting of the Sun by using helioseismic data. They found a mild value of $\Lambda_e \approx 0.37$ reproduced the measured data very well. Later, Molaro et al. (2012) and Fu et al. (2015) proposed a new scenario to explain the ${}^7\text{Li}$ depletion during the PMS. These authors suggested that a high-efficiency overshooting, mass-independent parameter, may cause a significant PMS ${}^7\text{Li}$ destruction, but then, in the late PMS, a residual accretion can restore ${}^7\text{Li}$ almost to the pristine value.

In this section, we take a further step in our model construction by introducing a simple scheme that purely explores the role of envelope overshooting. In particular, a milder value of the overshooting efficiency parameter is used during the evolution before it reaches the end of the MS. For the post-MS phases, a value of $\Lambda_e = 0.6$ is used based on the best-selected model on the CMD fitting and the onset’s location of thermohaline mixing above.

We computed several grids of models with different values of envelope-overshoot efficiency for the early evolution (from the beginning of the PMS to the end of the MS) and applied the efficiency $\Lambda_e = 0.6$ for the rest of the evolution. To avoid confusion, the prior value that applied to early-MS phases is noted as Λ_e^p . Primordial lithium, $A({}^7\text{Li}) = 2.69$, is adopted for the initial lithium abundance used in the models. For the sake of clarity regarding the trend of the observed abundances, especially in the region around the lithium peak on the sub-giant branch, we use abundance values averaged over luminosity bins (i.e. $d \log L =$

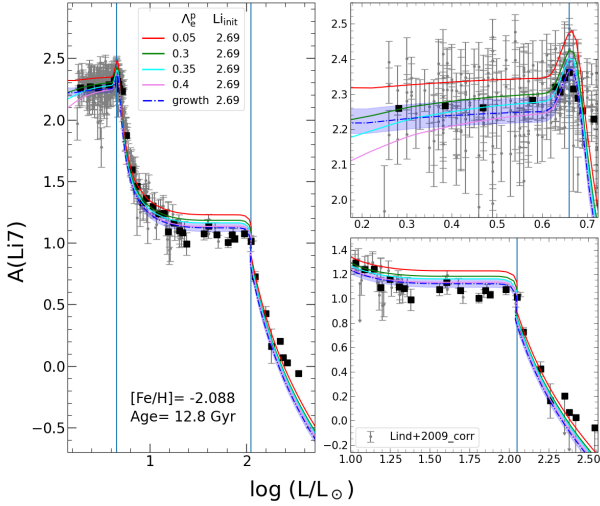


Fig. 10. Variation in ${}^7\text{Li}$ -abundance in average values (black squares) with our models of various overshooting efficiencies at the early evolution. The applied values of Λ_c^p and initial $A(\text{Li}^7)$ are indicated in the label. The two panels on the right-hand side focus on the plateau (top-panel) and the RGB bump region (bottom-panel), with the re-derived 3D+NLTE data being shown in grey dots. The shaded area marks the uncertainty coming from the primordial lithium, $A({}^7\text{Li}) = 2.69^{+0.04}_{-0.03}$ of the “growth” model.

0.1 dex for $\log L \leq 0.57$, 0.01 dex for $\log L = 0.57 - 0.65$, and 0.05 dex for the rest). Fig. 10 shows the averaged observed abundances and the predicted surface lithium abundances of models with different Λ_c^p . We also apply a shift of +0.05 dex in $\log L$ to the data in order to match the peak with the isochrones. The constrained age and metallicity are adopted from the CMD fitting above. The averaged plateau clearly favours a model with a low value of envelope overshooting, $\Lambda_c^p = 0.3-0.35$. However, the strength of the peak before the 1DU sets in identifies a best-fitting value, $\Lambda_c^p = 0.4$. This result is in good agreement with the calibration of Christensen-Dalsgaard et al. (2011).

We take one more step in relation to this aspect. As shown in Fig. 9, the colour bar shows a clear mass tendency of these stars, that is, higher mass stars have evolved to higher luminosities, while the Spite plateau shows an almost constant $A({}^7\text{Li})$. The low-mass PMS stars have deep convective zones after they leave their birthlines, and the lower the mass, the deeper the convective boundary the star will have. Meanwhile, the temperature at the base of the envelope during the first few Myrs of evolution is typically about $\sim 3 \times 10^6$ K depending on its initial mass. Lithium, in turn, is very fragile as the nuclear reaction rate of ${}^7\text{Li}(p, \alpha){}^4\text{He}$ is already efficient in this range of temperatures. Therefore, the destruction of lithium during this early phase becomes very sensitive to the efficiency of overshooting, since the latter increases the temperature at the base of the mixed envelope. The variation of envelope overshooting efficiency with initial mass was already introduced in Bressan et al. (2012), and recently Addari et al. (2024) required such a dependency to reproduce the non-monotonic behaviour of the initial-final mass relation reported in Marigo et al. (2020). In this work, we apply this dependency on initial mass for Λ_c^p . Within the mass range from $0.64-0.86 M_\odot$ with step mass of $0.02 M_\odot$, the corresponding applied value of $\Lambda_c^p = 0.05-0.60$ with a step of 0.05. This model is shown by the dash-dotted blue line, labelled as “growth”, in Fig. 10. It is evident that the new model reproduces the plateau, including the peak, quite well. However, we

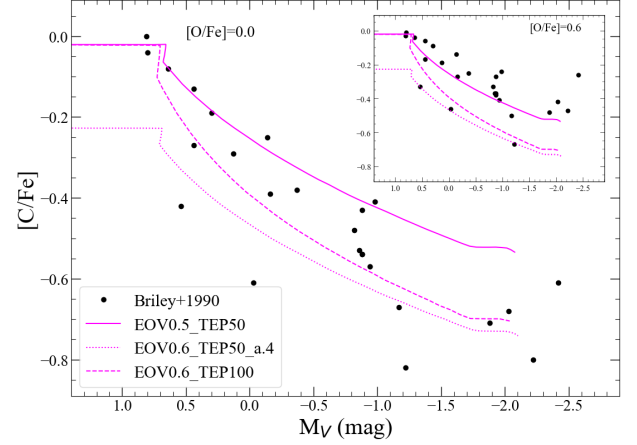


Fig. 11. Variation of ${}^{12}\text{C}$ abundance with absolute V -band magnitude. The best-fit isochrones in Fig. 8 are used in this plot together with the observed data from Briley et al. (1990), with two assumptions for oxygen enhancement ($[\text{O}/\text{Fe}] = 0.0$ and 0.6).

should emphasise that this new model is introduced to simply explore the impact of early-evolution variations of lithium before the onset of thermohaline mixing, while the effects of mixing processes on light elements such as lithium during the PMS and MS remains ambiguous (see Richard et al. 2005; Fu et al. 2015; Eggenberger et al. 2012; Dumont et al. 2021, and references therein).

Returning to the post-MS evolution, the averaged data display the renowned peak on the sub-giant branch (at $\log L/L_\odot = 0.66$) observed in previous works (Korn et al. 2007; Lind et al. 2009) and understood as a short dredge-up of lithium from layers into which this element had previously settled by atomic diffusion. At the same time, the average luminosity of three stars at the RGB bump location is $\log L/L_\odot = 2.05$. These two identifiable features are marked by the vertical lines in the figure panels. All our models demonstrate the fact that changing the overshooting efficiency does not change the location of the Li peak on the sub-giant branch. However, changing the overshooting efficiency changes the location of the RGB bump (see Fig. 9). This suggests a robust way to calibrate the value of envelope overshooting efficiency by using the relative distance between the peak feature of $A(\text{Li}^7)$ on the sub-giant branch and the location of the RGB bump, where lithium is about to be destroyed due to thermohaline mixing. This is a distance-independent method in the sense that the location of the RGB bump is measured relative to another feature of the same star cluster, which assures the robustness of this method. Indeed, the prediction of our model using the calibrated $\Lambda_c = 0.6$ shows the best fit to the data.

To conclude this subsection, we would like to emphasise that changing the efficiency of envelope overshooting at the early-MS phases does not change the photometry properties of the stars ($\log L$, $\log T_{\text{eff}}$). Therefore, our model attempts for the early evolutionary phases do not change our conclusions above. Indeed, our model only shows sizeable effects on the variation of light elements such as lithium during this evolution. Heavier elements such as ${}^{12}\text{C}$ and ${}^{13}\text{C}$ instead show no or very little effect in very low-mass models.

3.3. C-abundances

Besides lithium, carbon abundance is also commonly used to probe the internal mixing of RGB stars. As mentioned in

Sect. 2.5, the $^{12}\text{C}/^{13}\text{C}$ ratio is a more reliable calibrator than the ^{12}C abundance alone. However, due to the limitations of available isotopic data for carbon in NGC 6397, we can only carry out our comparison with the ^{12}C abundances. Fig. 11 shows the $A(^{12}\text{C})$ of 25 RGB stars in NGC 6397 by Briley et al. (1990) over-plotted with the three models that we showed in Fig. 9. To derive the absolute V -band magnitude, we apply the extinction coefficient from Correnti et al. (2018), namely $A_V = 0.76$ mag, to our isochrones in Fig. 11. As a matter of fact, the abundance data seems rather scattered, and our models with the values of thermohaline mixing efficiency $\alpha_{\text{th}} = 50$ to 100 seemingly cover the spread of the data. At this point, we recall from Sect. 2.5 (Fig. 4) that envelope overshooting does not play a significant role in the variation of carbon abundance.

We do not know the source of this spread in the observed data. One of the factors that could explain it is the multiple populations in this cluster (Lind et al. 2011; Milone et al. 2012; MacLean et al. 2018, and references therein). To support this argument, the sub-plot in Fig. 11 shows the measured $A(^{12}\text{C})$ by assuming the enhanced oxygen abundance, $[\text{O}/\text{Fe}] = 0.6$, reported in Briley et al. (1990). We see that our α -enhanced model fits the three stars at the lower limit of the spread very well. However, we should emphasise that a more detailed analysis would be needed to lead us to such a conclusion, and we reserve this topic for future works.

We also tested our models on the C abundance of another metal-poor GC, M92. We adopted the data from Bellman et al. (2001) and tried to fit them with our isochrones, $Z = 0.0001$, $t = 13$ Gyrs, and $A_V = 0.05$ mag. The result gave us an offset that was about ~ 0.2 dex higher than the data. We are not certain what causes this gap between the observed data and our isochrones, but we noticed that in their analysis, Bellman et al. (2001) reported different derived $[\text{C}/\text{Fe}]$ values by using models with different input oxygen abundances. In other words, the input $[\text{O}/\text{Fe}]$ apparently contributes to the uncertainty of the derived $[\text{C}/\text{Fe}]$ values. For example, in many cases in their Table 4, there is a difference of about 0.1 dex between models using $[\text{O}/\text{Fe}] = 0.00$ and 0.3. On this note, the recent analysis of globular clusters from the Apache Point Observatory Galactic Evolution Experiment (APOGEE) survey with the BACCHUS code by Mészáros et al. (2020) shows the oxygen abundance of M92 is rather high, > 0.6 dex. Therefore, we believe the inconsistency is due to the input $[\text{O}/\text{Fe}]$ that was assumed to derive the C abundances in Bellman et al. (2001). To conclude this section, we recognise that careful attention should be paid to the α elements in models when one uses C abundance to probe internal mixing in low-mass RGB stars. Alternatively, the $^{12}\text{C}/^{13}\text{C}$ ratio is more favourable, and we would like to explore this aspect in the near future.

4. Distance-independent calibration of Λ_e from seismic data of GC M4

Khan et al. (2018) have shown that a distance-independent calibration of the efficiency of envelope overshooting can be obtained by analysing the seismic properties of RGB bump stars. Here we perform a similar analysis using the available seismic data of the globular cluster M4 provided by Howell et al. (2022, hereafter H22).

Firstly, during the evolution along the RGB phase, low-mass stars make a ‘zig-zag’ path (or the RGB bump), and this is due to the interaction between the H-shell and the discontinuity. The encounter provides the H-shell with more fuel and thus leads to a temporary decrease in luminosity; shortly after, when the

equilibrium is restored, the luminosity rises again. This implies that stars accumulate at this region of the CMD, which creates the RGB bump. Besides that, the location of the RGB bump is strongly correlated to the efficiency parameter of envelope overshooting. In particular, the more extended the envelope, that is, the larger Λ_e , the earlier the encounter occurs and hence the fainter the RGB bump is. When these properties of the RGB bump are understood, the star count distribution becomes a powerful tool to calibrate the efficiency parameter of the envelope overshooting. For example, Fu et al. (2018) used the star count distribution in a small bin of magnitude to calibrate the luminosity function of GC 47 Tuc and obtained a best-fit value of $\Lambda_e = 0.5$. However, by using the magnitudes for such calibration, one has to cope with the uncertainty that comes from photometric properties such as distance modulus and dust extinction.

The seismic data sample provided in H22, which claims to be the largest seismic sample in a GC to date, contains seismic data for 59 red giant stars distributed below and above the location of the RGB bump. The observed seismic quantities, namely the frequency of maximum oscillation power (ν_{max}) and mean frequency separation of acoustic modes ($\Delta\nu$), can be expressed as functions of the intrinsic properties of the stars (see e.g. Ulrich 1986; Kjeldsen & Bedding 1995; Miglio et al. 2012),

$$\frac{\nu_{\text{max}}}{\nu_{\text{max},\odot}} = \left(\frac{M}{M_{\odot}}\right) \left(\frac{R}{R_{\odot}}\right)^{-2} \left(\frac{T_{\text{eff}}}{T_{\text{eff},\odot}}\right)^{-1/2}, \quad (5)$$

$$\frac{\Delta\nu}{\Delta\nu_{\odot}} = \left(\frac{M}{M_{\odot}}\right)^{1/2} \left(\frac{R}{R_{\odot}}\right)^{-3/2}, \quad (6)$$

where M , R , and T_{eff} are the stellar mass, radius, and effective temperature, respectively. In Eqs. (5) and (6), the solar values are provided in H22: $\nu_{\text{max},\odot} = 3090 \mu\text{Hz}$, $\Delta\nu_{\odot} = 135.1 \mu\text{Hz}$, $M_{\odot} = 1.989 \times 10^{33}$ g, $R_{\odot} = 6.9599 \times 10^{10}$ cm, and $T_{\text{eff},\odot} = 5772$ K.

The comparison between the observed seismic data of RGB bump stars with the corresponding one predicted by models on the basis of the above relations can thus provide another check on the robustness of the envelope overshooting model. Before proceeding with this test, we recall that the predicted seismic properties of RGB bump stars change with both the metallicity and age. To estimate these dependencies, we have calculated theoretical isochrones for the metallicity and age ranges suitable for the GC M4. M4 is a moderately metal-poor GC. In a recent analysis based on high-resolution ESO/VLT FLAMES spectroscopy of 35 RGB stars spreading from the lower branch to above the bump region, Nordlander et al. (2024) find a metallicity of $[\text{Fe}/\text{H}] = -1.13 \pm 0.07$, in excellent agreement with previous works (e.g. Mucciarelli et al. 2011; Monaco et al. 2012; Malavolta et al. 2014; Wang et al. 2017). The cluster is confirmed to have enhanced α elements; for example, Nordlander et al. (2024) obtain $[\text{O}/\text{Fe}] \sim 0.6$ dex, while Marino et al. (2008) give $[\alpha/\text{Fe}] = 0.39 \pm 0.05$ dex (see also Villanova & Geisler 2011; Yong et al. 2008). The age of M4 varies between 11–13 Gyr; for example, Tailo et al. (2022) estimate a range between 11–12 Gyr, while Wang et al. (2017) give 11.50 ± 0.38 Gyr, which agrees very well with McDonald & Zijlstra (2015), who find 11.81 ± 0.66 Gyr; Marín-Franch et al. (2009) claim an age of 12.65 ± 0.64 Gyr, while Hansen et al. (2002) derive an age of 12.7 ± 0.7 Gyr. We computed two initial metallicities, $Z = 0.001 - 0.002$, ($Y = 0.250, 0.252$ correspondingly), using the α -enhanced mixtures (Fu et al. 2018). The isochrones were then obtained with the TRILEGAL code for this purpose.

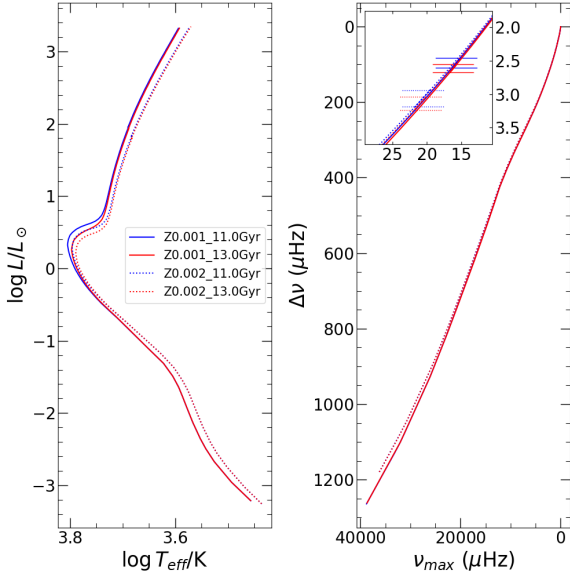


Fig. 12. Left: Hertzsprung–Russell diagram (HRD) of four selected isochrones, with metallicity spanning from 0.001–0.002 and age ranges from 11–13 Gyr. Right: Seismic diagram corresponding to the HRD on the left side. The inset is a zoom-in of the region of the RGB bump. The horizontal bars mark the maximum and minimum of the bump.

In Fig. 12, we show the conversion from the theoretical isochrones ($\log L$, $\log T_{\text{eff}}$) to the seismic diagram ($\Delta\nu$, ν_{max}), with the metallicity and age ranges suitable for the GC M4. Regarding the location of the RGB bump (insert panel), we find that changing the age from 11 to 13 Gyr affects $\Delta\nu$ by $\sim 0.1 \mu\text{Hz}$ and ν_{max} by $\sim 0.5 \mu\text{Hz}$. Instead, by changing the metallicity from $Z = 0.001$ to 0.002, the variation in $\Delta\nu$ is $\sim 0.5 \mu\text{Hz}$ and that of ν_{max} is $\sim 4.5 \mu\text{Hz}$. Thus, to obtain a sound calibration from M4 data, it is more important to determine its precise metallicity than its age.

To perform the seismic calibration of the RGB bump of M4, we need to identify that the H22 sample has no significant selection bias on the evolutionary stage. For this purpose, we cross-match H22 stars with the cluster member catalogue of Vasiliev & Baumgardt (2021) using Gaia Early Data Release 3 (EDR3) data. Fig. 13 shows the CMD of M4 in the Gaia EDR3/DR3 pass-bands, with data taken from Vasiliev & Baumgardt (2021). We only selected the stars that have a member probability larger than 0.95, and eliminated the horizontal branch stars for the sake of cleanliness. The 58 RGB stars from the H22 sample are indicated by the open circles. The stars were originally studied by H22 using Gaia DR2 photometry. Here, the Gaia DR3 information is obtained by cross-matching with the Gaia source_id provided by H22. We highlight the likely RGB bump stars of H22 with open blue circles and the remaining stars in H22 with open red circles (star M4RGB169 is excluded because it is not presented in the Gaia DR3 catalogue). A zoom-in on the H22 sample in the CMD around the RGB bump area is shown in the bottom-right panel of Fig. 13. In the top-right panel of Fig. 13, we show the G -magnitude function of RGB stars from Vasiliev & Baumgardt (2021, blue histogram) together with that of H22 seismic data (orange histogram). The magnitude of the RGB bump of the M4 Gaia member catalogue, $G_{\text{mag}} \sim 13$ mag, is marked by the grey arrow. The G -magnitude function of the H22 seismic data (orange histogram) presents a peak that is consistent with the Gaia member RGB bump. This is strong evidence that the

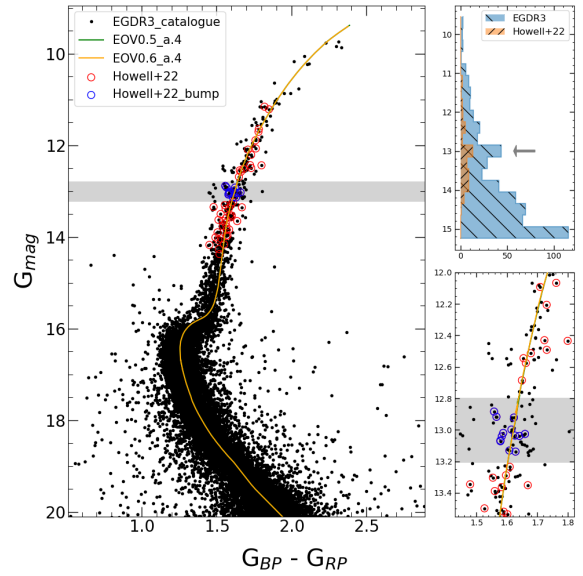


Fig. 13. Colour-magnitude diagram of M4 with data from the Gaia EDR3 catalogue (Vasiliev & Baumgardt 2021) with the isochrones shown in Fig. 14. The adopted parameters for the isochrones are 12.6 Gyr, $Z = 0.0015$, $(m - M)_0 = 11.35$ mag, and $A_v = 1.3$ mag. The open circles are stars from the Howell et al. (2022) sample. Top-right: Star count histogram on G_{mag} with a magnitude bin of 0.3 dex along the RGB. Bottom-right: Zoom-in of the RGB bump area.

H22 sample has no significant selection bias on the evolutionary stage compared to the Gaia Vasiliev & Baumgardt (2021) sample. With this evidence, we can safely use the H22 seismic data to calibrate the RGB bump stellar models.

We now compare the observed seismic properties of the H22 RGB stars with those predicted by assuming a different efficiency of envelope overshooting; we do this in Fig. 14. The top panel of Fig. 14 shows the histogram of star count distribution in ν_{max} with a step of 12 μHz . The bottom-right panel shows the $\Delta\nu$ histogram with a step of 1 μHz . The star count is normalised to its maximum value within the range, with the peak region referred to the distinguished RGB bump stars (blue circle). The theoretical luminosity function is computed by adopting an age of 12.6 Gyr (see Marín-Franch et al. 2009), and an initial metallicity that produces the measured metallicity of Nordlander et al. (2024), in the bump region. It should be mentioned that Nordlander et al. (2024) adopt Grevesse et al. (2007) solar compositions, while we adopt the compositions from Caffau et al. (2011). In other words, the rescaled metallicity due to the difference in solar reference composition is $[\text{Fe}/\text{H}] = -1.2$ dex. This value corresponds to $Z = 0.0015$ with our adopted $[\alpha/\text{Fe}] = 0.4$ mixture. The solid lines in Fig. 14 show the prediction from theoretical models with this metallicity, and with different values of envelope overshooting parameter. The computed model with α -enhanced mixture and $\Lambda_e = 0.6$ shows the best fit to the observed star count histogram, while the model with lower values, $\Lambda_e = 0.05$ (adopted from PARSEC v1.2S) and $\Lambda_e = 0.5$, predict a frequency of the bump that is too low to reproduce the observed data. It should be emphasised that this result holds for histograms performed in both $\Delta\nu$ and ν_{max} . We also check this best-fit model on the CMD as shown in Fig. 13, together with the model of $\Lambda_e = 0.5$ for comparison. The isochrones are applied with the adopted distance modulus $(m - M)_0 = 11.35$ mag (see Baumgardt & Vasiliev 2021), and

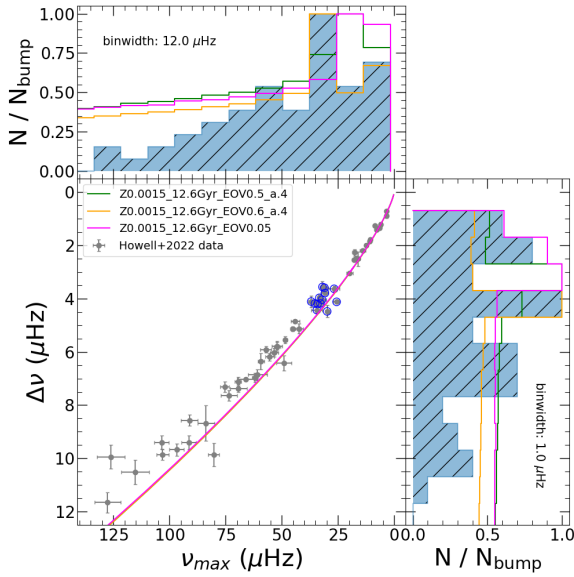


Fig. 14. Seismic diagram of 58 RGB stars in [Howell et al. \(2022\)](#). The selected isochrones with a variation of $\Lambda_e = 0.05, 0.5, 0.6$ are superimposed by solid lines. The distinguished excess stars in the H22 sample are circled in blue. Star count histograms on ν_{\max} and $\Delta\nu$ are shown in the top and right panels, correspondingly, in which the blue-hatched area indicates the H22 data and the lines represent model predictions.

extinction coefficient $A_v = 1.3$ mag (see [Hendricks et al. 2012](#), and references therein).

Furthermore, the multi-populations feature in the GC M4 has been studied in many works that have shown that the He content plays a key role. We know that one population is formed with He enrichment, while the other population has a normal He content that is compatible with the primordial value and located at the redder part of the cluster (e.g. [Villanova et al. 2012](#); [Valcarce et al. 2014](#); [D’Antona et al. 2022](#); [Costa et al. 2024](#)). However, a detailed analysis of the multiple populations in M4 is beyond the scope of this paper. However, it is worth mentioning that we compute our models by following the standard enrichment law for He content ([Bressan et al. 2012](#)). As a result, our isochrones give a good fit to the observed CMD, from the lower part of the MS up to the tip of the RGB. As an aside, we would like to mention that He content could be the cause of the mismatch on the lower RGB in [Fig. 14](#). However, this does not affect our conclusions since we focus on the upper part of the diagram where the RGB bump is located. A detailed analysis of this aspect is reserved for a coming work.

Finally, to conclude this section, we would like to stress that the model with $\Lambda_e = 0.6$ shows the best fit to the seismic star count distribution of GC M4. This result supports our finding in [Sect. 3](#). In other words, we have performed two independent calibrations, both distance- and reddening-independent, for the envelope overshooting parameter, and obtained good agreement with observations for $\Lambda_e = 0.6$. Although the two clusters we use for our calibrations have different metallicities, they are both in the low-metallicity domain $[\text{Fe}/\text{H}] = [-2.09, -1.21]$, that is, ~ 0.9 dex apart. We note that the brightness of the RGB bump of several GCs across a certain range of metallicity is well reproduced with a single envelope overshooting parameter as stated in [Fu et al. \(2018\)](#) (see their [Fig. 14](#), $[\text{Fe}/\text{H}] \sim [-1.3, -0.75]$; see also [Khan et al. 2018](#)). Our results point in the same direction, but for a lower-metallicity domain.

5. Summary and conclusions

In this paper, we first present the implementation of thermohaline mixing in the PARSEC code, and second the interplay between thermohaline mixing and envelope overshooting in low-mass stars. We explore the effects of these mixing processes on the surface abundance of lithium and carbon in [Sect. 2.5](#), together with variations in the adopted chemical mixtures. The efficiency parameters of these processes control the amount of abundances measurable at the stellar surface. Using [2012AJ....144...25H](#) observed data on two well-studied globular clusters (NGC 6397 and M4), we performed calibrations on the efficiency of the thermohaline mixing parameter, α_{th} , and on the envelope overshooting parameter, Λ_e , in [Sects. 3](#) and [4](#).

For theoretical models, we used the most recent version of the PARSEC code ([Costa et al. 2019b](#); [Nguyen et al. 2022](#)) with the implemented thermohaline mixing. Four sets of initial metallicity, $Z = 0.0001, 0.0002, 0.001, 0.002$, were computed, with variation in the efficiency parameters. Each metallicity set contains 14 stellar tracks with masses spanning from $0.64\text{--}0.94 M_{\odot}$. The corresponding isochrones were then produced using the TRILEGAL code with the adoption of very-low-mass models from the previous PARSEC v1.2s. Then, they were complemented with the YBC bolometric correction tables for the benefit of our calibrations.

In this work, thermohaline mixing is treated as a diffusive process, and we follow the standard scheme of [Charbonnel & Zahn \(2007a\)](#) and [Cantiello & Langer \(2010\)](#) to model it. We carefully study the impact of thermohaline mixing on evolution and changes in chemical abundances.

We performed calibration on the thermohaline mixing efficiency parameter based on the observed ${}^7\text{Li}$ abundances of stars in GC NGC 6397 from [Lind et al. \(2009\)](#). To work with the latest 3D+NLTE abundances, we re-derived the inferred abundances from the lines’ equivalent widths by using the BREIDABLIK package ([Wang et al. 2021](#)). A relatively small value of $\alpha_{\text{th}} = 50$ was obtained to reproduce the lithium abundance of three stars above the RGB bump. Moreover, our attempted models with smaller envelope overshooting efficiencies for the PMS and MS phases, and $\Lambda_e = 0.6$ for the post-MS, together with the thermohaline efficiency parameter $\alpha_{\text{th}} = 50$, gives the best fit to the 3D+NLTE lithium abundances of GC NGC 6397, from the Spite-plateau to the RGB stars. Furthermore, the luminosity difference between the Li-peak on the sub-giant and the onset of thermohaline mixing at the RGB bump implies a robust calibration with $\Lambda_e = 0.6$.

An independent and alternative approach to calibrate the efficiency of envelope overshooting was done by using the seismology data of GC M4. In this analysis, we focus on the star count distribution in both the frequency of maximum oscillation power, ν_{\max} , and the mean frequency separation of acoustic modes, $\Delta\nu$, to draw our conclusion on the best-fitting value for Λ_e . As a result, we find that $\Lambda_e = 0.6$ is required to reproduce the accumulation of stars at the RGB bump of M4. This result agrees with the former one, and thus strengthens our conclusion.

Finally, we would like to stress that even though rotation has been implemented in the PARSEC code ([Costa et al. 2019b](#); [Nguyen et al. 2022](#)), we do not consider it in the present work. We focus on the effect of convective envelope overshooting and thermohaline mixing along the post-MS phases. The impact of rotation on thermohaline mixing has already been investigated in the literature (e.g. [Charbonnel & Lagarde 2010](#); [Lagarde et al. 2011](#)). Moreover, [Maeder et al. \(2013\)](#) pointed out that the horizontal turbulence in rotating stars can inhibit thermohaline

mixing, which led to an even more complex scenario. A project combining all these effects is deferred to the future.

The re-derived 3D+NLTE lithium abundance of NGC 6397, together with the stellar tracks of our best-fit models that are presented in this paper, can be archived at the dedicated ZENODO dataset⁹. The isochrones with different photometric pass-bands can be provided upon request.

Acknowledgements. The authors are in deepest sorrow with the passing of Prof. Paola Marigo on October 20, 2024. We wish to express our gratitude for her dedications and guidance over the years. We thank the anonymous referee for the insightful comments and suggestions to improve the paper. CTN also thanks Madeline Howell for providing useful seismic data information. This project has received funding from the European Union’s Horizon 2020 research and innovation programme under grant agreement No 101008324 (ChETEC-INFRA). AB acknowledges the Italian Ministerial grant PRIN2022, “Radiative opacities for astrophysical applications”, no. 2022NEXMP8. GC acknowledges support from the Agence Nationale de la Recherche grant POPSYCLE number ANR-19-CE31-0022. X.F. acknowledges the support of the National Natural Science Foundation of China (NSFC) No. 12203100 and the China Manned Space Project with NO.CMS-CSST-2021-A08. AJK acknowledges support by the Swedish National Space Agency (SNSA)

References

Addari, F., Marigo, P., Bressan, A., et al. 2024, *ApJ*, 964, 51
 Aguilera-Gómez, C., Monaco, L., Mucciarelli, A., et al. 2022, *A&A*, 657, A33
 Aguilera-Gómez, C., Jones, M. I., & Chanamé, J. 2023, *A&A*, 670, A73
 Ahumada, J. A., Arellano Ferro, A., Bustos Fierro, I. H., et al. 2021, *New Astron.*, 88, 101607
 Alongi, M., Bertelli, G., Bressan, A., & Chiosi, C. 1991, *A&A*, 244, 95
 Baumgardt, H., & Vasiliev, E. 2021, *MNRAS*, 505, 5957
 Baumgardt, H., Hilker, M., Sollima, A., & Bellini, A. 2019, *MNRAS*, 482, 5138
 Beers, T. C., & Christlieb, N. 2005, *ARA&A*, 43, 531
 Bellman, S., Briley, M. M., Smith, G. H., & Claver, C. F. 2001, *PASP*, 113, 326
 Bertelli, G., Betto, R., Bressan, A., et al. 1990, *A&AS*, 85, 845
 Bertelli, G., Girardi, L., Marigo, P., & Nasi, E. 2008, *A&A*, 484, 815
 Bonifacio, P. 2002, *A&A*, 395, 515
 Bressan, A. G., Chiosi, C., & Bertelli, G. 1981, *A&A*, 102, 25
 Bressan, A., Marigo, P., Girardi, L., et al. 2012, *MNRAS*, 427, 127
 Briley, M. M., Bell, R. A., Hoban, S., & Dickens, R. J. 1990, *ApJ*, 359, 307
 Brown, T. M., Casertano, S., Strader, J., et al. 2018, *ApJ*, 856, L6
 Caffau, E., Ludwig, H. G., Steffen, M., Freytag, B., & Bonifacio, P. 2011, *Sol. Phys.*, 268, 255
 Cantiello, M., & Langer, N. 2010, *A&A*, 521, A9
 Charbonnel, C., & Lagarde, N. 2010, *A&A*, 522, A10
 Charbonnel, C., & Primas, F. 2005, *A&A*, 442, 961
 Charbonnel, C., & Zahn, J. P. 2007a, *A&A*, 467, L15
 Charbonnel, C., & Zahn, J. P. 2007b, *A&A*, 476, L29
 Charbonnel, C., Brown, J. A., & Wallerstein, G. 1998, *A&A*, 332, 204
 Chen, Y., Girardi, L., Bressan, A., et al. 2014, *MNRAS*, 444, 2525
 Chen, Y., Girardi, L., Fu, X., et al. 2019, *A&A*, 632, A105
 Christensen-Dalsgaard, J., Monteiro, M. J. P. F. G., Rempel, M., & Thompson, M. J. 2011, *MNRAS*, 414, 1158
 Coc, A., Goriely, S., Xu, Y., Saimpert, M., & Vangioni, E. 2012, *ApJ*, 744, 158
 Coc, A., Uzan, J.-P., & Vangioni, E. 2014, *JCAP*, 2014, 050
 Cohen, R. E., Hempel, M., Mauro, F., et al. 2015, *AJ*, 150, 176
 Correnti, M., Gennaro, M., Kalirai, J. S., Cohen, R. E., & Brown, T. M. 2018, *ApJ*, 864, 147
 Costa, G., Girardi, L., Bressan, A., et al. 2019a, *A&A*, 631, A128
 Costa, G., Girardi, L., Bressan, A., et al. 2019b, *MNRAS*, 485, 4641
 Costa, G., Bressan, A., Mapelli, M., et al. 2021, *MNRAS*, 501, 4514
 Costa, G., Dumont, T., Lançon, A., et al. 2024, *A&A*, 690, A22
 Costa, G., Shepherd, K. G., Bressan, A., et al. 2025, *A&A*, 694, A193
 D’Antona, F., Milone, A. P., Johnson, C. I., et al. 2022, *ApJ*, 925, 192
 Dotter, A., Sarajedini, A., Anderson, J., et al. 2010, *ApJ*, 708, 698
 Dumont, T., Palacios, A., Charbonnel, C., et al. 2021, *A&A*, 646, A48
 Eggenberger, P., Haemmerlé, L., Meynet, G., & Maeder, A. 2012, *A&A*, 539, A70
 Eggleton, P. P., Dearborn, D. S. P., & Lattanzio, J. C. 2006, *Science*, 314, 1580
 Frebel, A., & Norris, J. E. 2015, *ARA&A*, 53, 631
 Fu, X., Bressan, A., Molaro, P., & Marigo, P. 2015, *MNRAS*, 452, 3256
 Fu, X., Bressan, A., Marigo, P., et al. 2018, *MNRAS*, 476, 496

Girardi, L., Groenewegen, M. A. T., Hatziminaoglou, E., & da Costa, L. 2005, *A&A*, 436, 895
 Gontcharov, G. A., Bonatto, C. J., Rytulina, O. S., et al. 2023, *MNRAS*, 526, 5628
 Gratton, R. G., Sneden, C., Carretta, E., & Bragaglia, A. 2000, *A&A*, 354, 169
 Gratton, R. G., Bragaglia, A., Carretta, E., et al. 2003, *A&A*, 408, 529
 Grevesse, N., Asplund, M., & Sauval, A. J. 2007, *Space Sci. Rev.*, 130, 105
 Hansen, B. M. S., Brewer, J., Fahlman, G. G., et al. 2002, *ApJ*, 574, L155
 Hansen, B. M. S., Anderson, J., Brewer, J., et al. 2007, *ApJ*, 671, 380
 Hendricks, B., Stetson, P. B., VandenBerg, D. A., & Dall’Ora, M. 2012, *AJ*, 144, 25
 Henkel, K., Karakas, A. I., & Lattanzio, J. C. 2017, *MNRAS*, 469, 4600
 Henkel, K., Karakas, A. I., Casey, A. R., Church, R. P., & Lattanzio, J. C. 2018, *ApJ*, 863, L5
 Howell, M., Campbell, S. W., Stello, D., & De Silva, G. M. 2022, *MNRAS*, 515, 3184
 Khan, S., Hall, O. J., Miglio, A., et al. 2018, *ApJ*, 859, 156
 Kippenhahn, R., Ruschenplatt, G., & Thomas, H. C. 1980, *A&A*, 91, 175
 Kjeldsen, H., & Bedding, T. R. 1995, *A&A*, 293, 87
 Komatsu, E., Smith, K. M., Dunkley, J., et al. 2011, *ApJS*, 192, 18
 Korn, A. J., Grundahl, F., Richard, O., et al. 2007, *ApJ*, 671, 402
 Lagarde, N., Charbonnel, C., Decressin, T., & Hageberg, J. 2011, *A&A*, 536, A28
 Lind, K., Primas, F., Charbonnel, C., Grundahl, F., & Asplund, M. 2009, *A&A*, 503, 545
 Lind, K., Charbonnel, C., Decressin, T., et al. 2011, *A&A*, 527, A148
 MacLean, B. T., Campbell, S. W., De Silva, G. M., et al. 2018, *MNRAS*, 475, 257
 Maeder, A., Meynet, G., Lagarde, N., & Charbonnel, C. 2013, *A&A*, 553, A1
 Malavolta, L., Sneden, C., Piotto, G., et al. 2014, *AJ*, 147, 25
 Marigo, P., Girardi, L., Bressan, A., et al. 2017, *ApJ*, 835, 77
 Marigo, P., Cummings, J. D., Curtis, J. L., et al. 2020, *Nat. Astron.*, 4, 1102
 Marín-Franch, A., Aparicio, A., Piotto, G., et al. 2009, *ApJ*, 694, 1498
 Marino, A. F., Villanova, S., Piotto, G., et al. 2008, *A&A*, 490, 625
 McDonald, I., & Zijlstra, A. A. 2015, *MNRAS*, 448, 502
 Mészáros, S., Masseron, T., García-Hernández, D. A., et al. 2020, *MNRAS*, 492, 1641
 Miglio, A., Brogaard, K., Stello, D., et al. 2012, *MNRAS*, 419, 2077
 Milone, A. P., Marino, A. F., Piotto, G., et al. 2012, *ApJ*, 745, 27
 Molaro, P., Bressan, A., Barbieri, M., Marigo, P., & Zaggia, S. 2012, *Mem. Soc. Astron. It. Suppl.*, 22, 233
 Monaco, L., Villanova, S., Bonifacio, P., et al. 2012, *A&A*, 539, A157
 Mucciarelli, A., Salaris, M., Lovisi, L., et al. 2011, *MNRAS*, 412, 81
 Nataf, D. M., Gould, A. P., Pinsonneault, M. H., & Udalski, A. 2013, *ApJ*, 766, 77
 Nguyen, C. T., Costa, G., Girardi, L., et al. 2022, *A&A*, 665, A126
 Nordlander, T., Gruyters, P., Richard, O., & Korn, A. J. 2024, *MNRAS*, 527, 12120
 Placco, V. M., Frebel, A., Beers, T. C., & Stancliffe, R. J. 2014, *ApJ*, 797, 21
 Planck Collaboration XVI. 2014, *A&A*, 571, A16
 Reid, I. N., & Gizis, J. E. 1998, *AJ*, 116, 2929
 Richard, O., Michaud, G., & Richer, J. 2005, *ApJ*, 619, 538
 Smith, G. H., & Tout, C. A. 1992, *MNRAS*, 256, 449
 Spite, F., & Spite, M. 1982a, *A&A*, 115, 357
 Spite, M., & Spite, F. 1982b, *Nature*, 297, 483
 Spite, M., & Spite, F. 2010, in *Light Elements in the Universe*, eds. C. Charbonnel, M. Tosi, F. Primas, & C. Chiappini, 268, 201
 Stancliffe, R. J. 2009, *MNRAS*, 394, 1051
 Stancliffe, R. J., Church, R. P., Angelou, G. C., & Lattanzio, J. C. 2009, *MNRAS*, 396, 2313
 Tailo, M., Milone, A. P., Lagioia, E. P., et al. 2020, *MNRAS*, 498, 5745
 Tailo, M., Corsaro, E., Miglio, A., et al. 2022, *A&A*, 662, L7
 Ulrich, R. K. 1972, *ApJ*, 172, 165
 Ulrich, R. K. 1986, *ApJ*, 306, L37
 Valcarce, A. A. R., Catelan, M., Alonso-García, J., Cortés, C., & De Medeiros, J. R. 2014, *ApJ*, 782, 85
 Valcin, D., Bernal, J. L., Jimenez, R., Verde, L., & Wandelt, B. D. 2020, *JCAP*, 2020, 002
 VandenBerg, D. A., Brogaard, K., Leaman, R., & Casagrande, L. 2013, *ApJ*, 775, 134
 Vasiliev, E., & Baumgardt, H. 2021, *MNRAS*, 505, 5978
 Viallet, M., Meakin, C., Prat, V., & Arnett, D. 2015, *A&A*, 580, A61
 Villanova, S., & Geisler, D. 2011, *A&A*, 535, A31
 Villanova, S., Geisler, D., Piotto, G., & Gratton, R. G. 2012, *ApJ*, 748, 62
 Wang, Y., Primas, F., Charbonnel, C., et al. 2017, *A&A*, 607, A135
 Wang, E. X., Nordlander, T., Asplund, M., et al. 2021, *MNRAS*, 500, 2159
 Yong, D., Lambert, D. L., Paulson, D. B., & Carney, B. W. 2008, *ApJ*, 673, 854

⁹ <https://doi.org/10.5281/zenodo.13283724>